Bull. Mater. Sci., Vol. 37, No. 3, May 2014, pp. 407–416. © Indian Academy of Sciences.

Structural study of nanosized yttrium-doped $CaMnO_3$ perovskites

J ZAGORAC[a,*], A ZARUBICA[b], A RADOSAVLJEVIC-MIHAJLOVIC[a], D ZAGORAC[c] and B MATOVIC[a]

[a]Materials Science Laboratory, Institute of Nuclear Sciences Vinca, Belgrade University, P. O. Box 522, 11001 Belgrade, Serbia
[b]Department of Chemistry, University of Nis, Visegradska 33, 18000 Nis, Serbia
[c]Max Planck Institute for Solid State Research, Heisenbergstr. 1, 70569, Stuttgart, Germany

MS received 29 April 2013; revised 12 June 2013

Abstract. Nanostructured compounds with general formula $Ca_{1-x}Y_xMnO_3$ ($0 \le x \le 1$) were synthesized by modified glycine nitrate procedure. In the next step, we have investigated crystal structure and microstructure of the synthesized samples using X-ray methods and Rietveld analysis. Focus of this research was the structural stability of the yttrium-doped $CaMnO_3$ perovskite phases, which crystallize in orthorhombic space group *Pnma*. We observed that the unit cell volumes of the investigated compounds increase proportionally with yttrium amount. Furthermore, we investigated the influence of yttrium amount on Mn–O bond angles and distances, tilting of MnO_6 octahedra and deformation due to the presence of Jahn–Teller distortion around Mn^{3+} cation. In order to estimate effective coordination of *A* and *B* sites, bond valence calculations (BVC) were performed for *A* and *B* site cations. Finally, the photoelectron spectroscopy (XPS) method was applied in order to follow yttrium concentration in the perovskite phases.

Keywords. Nanostructures; ceramics; photoelectron spectroscopy; X-ray diffraction; crystal structure.

1. Introduction

The perovskite structure type, ABO_3 is one of the most frequently encountered in solid-state inorganic chemistry due to the ability to host a variety of elements at both cation sites (Mitchell 2002). Substitution of cations of different size at *A* and *B* sites reduces symmetry from the cubic aristotype $Pm\bar{3}m$ to tetragonal, orthorhombic and monoclinic derivatives. Substitutions of cations of similar size in distorted derivatives commonly does not cause the change in space group but may result in a change of cell parameters, tilt angles of BO_6 polyhedra and displacement of *A* cations (Mitchell and Liferovich 2005). These changes may result in significant variations of physical properties.

There is a large number of scientific and industrial application of $CaMnO_3$-based compounds. Generally, they are used as electrode and connector materials for high temperature SOFC (Vecherskii *et al* 2002). $CaMnO_3$ based ceramics are interesting for their good electrical conductivity as well as for their magnetic properties. Doped perovskite manganites, with a general formula of $A_x^{2+}RE_{1-x}^{3+}Mn_x^{4+}Mn_{1-x}^{3+}O_x^{2-}$ (A, alkali earth element; RE, rare earth element), have attracted considerable interest due to their colossal magnetoresistance and acceptable levels of electrical conductivity for cathode materials used for solid oxide fuel cells (Raveau *et al* 1998). It was observed that the substitution of trivalent rare earth cation such as Y^{3+} for Ca^{2+} in the parent $CaMnO_3$ compound causes the reduction of Mn^{4+} to Mn^{3+} (Nagabhushana *et al* 2005). Presence of trivalent Mn introduces Jahn–Teller effect and distortion of the coordination polyhedra (Mitchell 2002). $Ca_{1-x}Y_xMnO_3$ has an orthorhombic perovskite-type structure and crystallizes in the space group *Pnma* (Aliaga *et al* 2001). According to Aliaga *et al* (2001), it is not possible to form $Ca_{1-x}Y_xMnO_3$ solid solution for every *x* value. For $x > 0{\cdot}8$ yttrium segregates since its solubility limit is reached.

Calcium manganite based compounds, independent of the application, should be developed in the way to satisfy the demands for low cost materials. Consequently, the preparation of nanometric size powders that ensures sintering at low temperatures, is of great interest (Boskovic *et al* 2008).

2. Experimental

Powders with nominal composition: $CaMnO_3$ (Ca100), $Ca_{0{\cdot}95}Y_{0{\cdot}05}MnO_3$ (Ca95), $Ca_{0{\cdot}85}Y_{0{\cdot}15}MnO_3$ (Ca85), $Ca_{0{\cdot}75}Y_{0{\cdot}25}MnO_3$ (Ca75), $Ca_{0{\cdot}5}Y_{0{\cdot}5}MnO_3$ (Ca50), $Ca_{0{\cdot}25}Y_{0{\cdot}75}MnO_3$ (Ca25) and $YMnO_3$ (Y100) were synthesized using a modified glycine nitrate process (MGNP) (Boskovic *et al* 2007; Dukic *et al* 2009). After the synthesis, the obtained ashes were calcined at 800 °C for 2 h.

*Author for correspondence (dukicjelena@yahoo.com)

The phase analysis of the synthesized powders was performed by X-ray powder diffraction (XRPD) on a Siemens D500 diffractometer using CuKα radiation, scintillation counter, $\theta/2\theta$-coupling reflection mode (2θ range: 10–90°). In order to derive the relevant structural parameters, experimental data for Rietveld refinement were taken afterwards in the same 2θ range with a step width of 0·025°2θ and 5 s per step. Structural analysis was carried out using Rietveld refinement and the program FullProf (Rodriguez-Carvajal 1990). Refinement of the crystalline phases obtained under experimental conditions was performed in order to investigate the amount of yttrium incorporated in the structure and its influence on unit cell parameters, unit cell volume and average bond distances. It turned out that the two phase compositions for Ca100, Ca95, Ca50 and Ca25 powders were obtained under mentioned conditions, while Ca85 and Ca75 turned to be single phase. Quantitative phase and microstructure size–strain analyses were performed as well.

The XPS spectra were recorded by an electron spectrometer (AXIS ULTRA, Kratos, UK) using monochromated AlKα radiation (1486·58 eV). To remove surface contaminants, the sample's surfaces were sputtered with high purity argon for 10 min. The binding energy was determined taking C (1*s*) line at 284·8 eV as reference. The peak profiles were fitted with a Voigt function.

3. Results and discussion

X-ray analysis showed two phase composition for Ca100, Ca95, Ca50 and Ca25 samples (table 1). Phase with perovskite structure type is dominant in all synthesized samples. As a second phase in the samples Ca100, Ca95 and Ca50, marokite ($CaMn_2O_4$) occurs with amounts of 5·8(1) wt%, 0·1(1) wt% and 4·4(2) wt%, respectively.

Marokite, $CaMn_2O_4$ is a naturally occurring mineral and it is orthorhombic, space group, *Pbcm*. The unit cell parameters determined from X-ray data are $a = 3{\cdot}1611(2)$; $b = 10{\cdot}0007(6)$; $c = 9{\cdot}6771(4)$ Å, in the Ca100 sample, in which its amount is the highest. Manganese ions are in the 3+ oxidation state and in a general position (8*e*), calcium in a mirror position (4*d*) and oxygen in three different sites (4*c*, 4*d* and 8*e*). Manganese is octahedrally coordinated, with octahedra sharing edges and corners (figure 1). The three-dimensional network of octahedra provides 8-coordinated sites for the larger calcium atoms (Mueller and Roy 1974). In addition, marokite is also identified as a minor impurity in the La-doped $CaMnO_3$ (Ling *et al* 2001). As a second phase in the Ca25 sample, YMn_2O_5 is observed and makes 8·0(3) wt%. It seems that yttrium solubility limit is reached for $x = 0{\cdot}75$, what is in a good agreement with previous studies (Aliaga *et al* 2001). YMn_2O_5 crystallizes in the $DyMn_2O_5$ structure type with orthorhombic space group symmetry *Pbam* and four formula units per unit cell. Refined unit cell parameters are: $a = 7{\cdot}2792(5)$, $b = 8{\cdot}6070(4)$; and $c = 5{\cdot}636(2)$. For the manganese atoms, two distinct Wyckoff sites (4*f* and 4*h*) exist in the unit cell: 4*f* with octahedral and 4*h* with pyramidal coordination of oxygens with formal oxidation states of +4 and +3, respectively (Wunderlich *et al* 2010). While the octahedra form edge-sharing chains along the crystallographic *c* axis, the tetragonal pyramids form units of two, connecting chains of octahedra by corners (figure 2). The yttrium atoms are coordinated by oxygen atoms of both these polyhedra forming distorted scalenohedra.

$YMnO_3$ does not form perovskite structure type since its cation is too small and leads to instability of the perovskite structure (Woodward *et al* 1998; Hibble *et al* 1999; Dlouha *et al* 2002; Zagorac *et al* 2010). At atmospheric pressure $YMnO_3$ crystallizes in hexagonal structure (space group *P*63*cm*) (Lukaszewicz and Karut-Kalicinska 1974; Van Aken *et al* 2001) and upon annealing under high pressures can be converted into the orthorhombic phase (Iliev *et al* 1998). Structure of hexagonal $YMnO_3$ is shown in figure 3. A solid solution $Ca_{1-x}Y_xMnO_3$ is found in the range of $0 = x < 0.75$ and segregation of $YMnO_3$ occurs for $x > 0{\cdot}75$ (Vega *et al* 2001).

Rietveld refinement revealed that all perovskite phases in investigated samples are orthorhombic with space group *Pnma*. Based on the relation between unit cell parameters: $b/\sqrt{2} > c$ and $c < a$ (table 1), only the perovskite phase in the sample Ca100 has orthorhombic $GdFeO_3$ type of structure (*O* type) which is one of the most common structures adopted by perovskite compounds, while other perovskite phases exhibit $REMnO_3$ (RE = La–Dy) or *O*′ type of the perovskite structure. The large cations, Ca and Y occupy the 4*c* (*x*, 1/4, *z*) position and the oxygen atoms are in two non-equivalent positions: O(1) at 4*c* (*x*, 1/4, *z*) and O(2) at 8*d* (*x*, *y*, *z*) (Blasco *et al* 1996). Refined positions for atoms are given in table 1. The results of refined unit cell parameters, unit cell volume and occupation factors are also given in table 1.

Influence of yttrium content on unit cell volumes and parameters *a*, *b* and *c* is shown in figure 4. Unit cell volume, as well as parameter *a* of the unit cell, increase with Y amount, while parameters *b* and *c* seem to be unchanged. The difference in the unit cell parameters and consequently in the unit cell volume are the result of the different amount of Y in each of these phases. According to Shannon for Ca^{2+} with CN = 12 ionic radius is 1·34 Å, and for Y^{3+} (CN = 8) is 1·019 Å (Shannon 1976). The exchange of Ca^{2+} with smaller cation results in increasing of unit cell parameters, which is not expected. The partial substitution of divalent Ca^{2+} by trivalent Y^{3+} is balanced by the reduction of equivalent amount of Mn valence states from Mn^{4+} to Mn^{3+} and the creation of oxygen vacancies, as well. The increase of unit cell parameters is therefore the result of Mn valence states reduction from Mn^{4+} (ionic radii in coordination VI is 0·53 Å) to Mn^{3+} (ionic radii in coordination VI is 0·645 Å). The doping of

Table 1. Nominal- and refined-phase compositions, amount of second phases and refined structural parameters for investigated perovskite phases.

Sample		Ca100	Ca95	Ca85	Ca75	Ca50	Ca25
Nominal composition		$CaMnO_3$	$Ca_{0.95}Y_{0.05}MnO_3$	$Ca_{0.85}Y_{0.15}MnO_3$	$Ca_{0.75}Y_{0.25}MnO_3$	$Ca_{0.5}Y_{0.5}MnO_3$	$Ca_{0.25}Y_{075}MnO_3$
% second phase		5·8(1) $CaMn_2O_4$	0·1(1) $CaMn_2O_4$	–	–	4·4(2) $CaMn_2O_4$	8·0(3) YMn_2O_5
Phase composition		$CaMnO_3$	$Ca_{0.94}Y_{0.06}MnO_3$	$Ca_{0.85}Y_{0.15}MnO_3$	$Ca_{0.78}Y_{0.22}MnO_3$	$Ca_{0.54}Y_{0.46}MnO_3$	$Ca_{0.3}Y_{0.7}MnO_3$
a (Å)		5·2808(3)	5·3057(2)	5·3324(2)	5·3598(2)	5·4744(2)	5·6088(3)
b (Å)		7·4591(7)	7·4701(4)	7·4786(3)	7·4812(3)	7·4495(2)	7·4437(4)
c (Å)		5·2743(5)	5·2805(3)	5·2882(2)	5·3004(3)	5·3093(2)	5·2832(3)
V(Å^3)		207·75(3)	209·29(2)	210·89(2)	212·53(3)	216·53(2)	220·57(2)
Occ			0·470(3)	0·426(3)	0·389(3)	0·271(6)	0·15(1)
			0·030(3)	0·074(3)	0·111(3)	0·229(6)	0·35(1)
$b/\sqrt{2}$		5·2744	5·2822	5·2882	5·2900	5·2677	5·2635
Ca	x	0·037(1)	0·0325(7)	0·0388(5)	0·0413(5)	0·0547(4)	0·0676(6)
	y	0·25	0·25	0·25	0·25	0·25	0·25
	z	0·001(4)	–0·010(2)	–0·007(2)	–0·009(1)	–0·0118(7)	–0·0128(9)
Mn	x	0	0	0	0	0	0
	y	0	0	0	0	0	0
	z	0·5	0·5	0·5	0·5	0·5	0·5
O1	x	0·489(3)	0·490(3)	0·4839(2)	0·486(2)	0·466(2)	0·473(3)
	y	0·25	0·25	0·25	0·25	0·25	0·25
	z	–0·064(5)	0·071(5)	0·067(3)	0·074(3)	0·099(3)	0·102(3)
O2	x	0·214(2)	0·287(3)	0·291(2)	0·299(2)	0·291(2)	0·290(2)
	y	–0·043(3)	0·029(3)	0·036(2)	0·034(2)	0·045(1)	0·051(2)
	z	–0·212(2)	–0·286(3)	–0·289(2)	–0·291(2)	–0·293(2)	–0·293(2)

$CaMnO_3$ at Ca^{2+} sites with trivalent Y^{3+} ions introduces electrons and due to charge compensation, the formation of Mn^{3+} takes place, which means that formula can be represented as $Ca_{1-x}Y_xMn^{4+}_{1-x}Mn^{3+}_xO_3$.

The results of Ca and Y occupation factors refinement (table 1) indicate that the perovskite phase in the Ca95 sample has the composition $Ca_{0.94}Y_{0.06}MnO_3$, and in samples Ca85, Ca75, Ca50 and Ca25 compositions are $Ca_{0.85}Y_{0.15}MnO_3$, $Ca_{0.78}Y_{0.22}MnO_3$, $Ca_{0.54}Y_{0.46}MnO_3$ and $Ca_{0.30}Y_{0.70}MnO_3$, respectively. Compositions of the perovskite phases calculated from occupation factors are in good agreement with nominal compositions.

The change of Mn valence states can be investigated through the average Mn–O bond distances in the octahedra. The average bond distance ⟨Mn–O⟩ in undoped $CaMnO_3$ is 1·899 Å (Aliaga *et al* 2001), and in perovskite

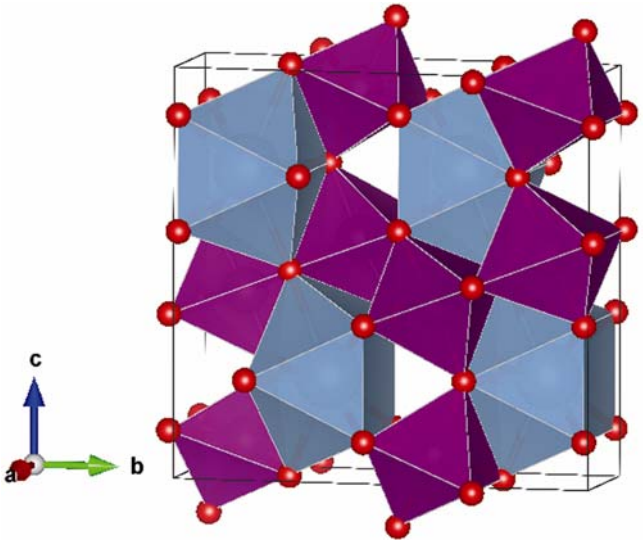

Figure 1. Structure of marokite, $CaMn_2O_4$. 6-fold coordinated Mn^{3+} and 8-fold coordinated Ca^{2+} is represented with violet octahedra and grey polyhedra, respectively.

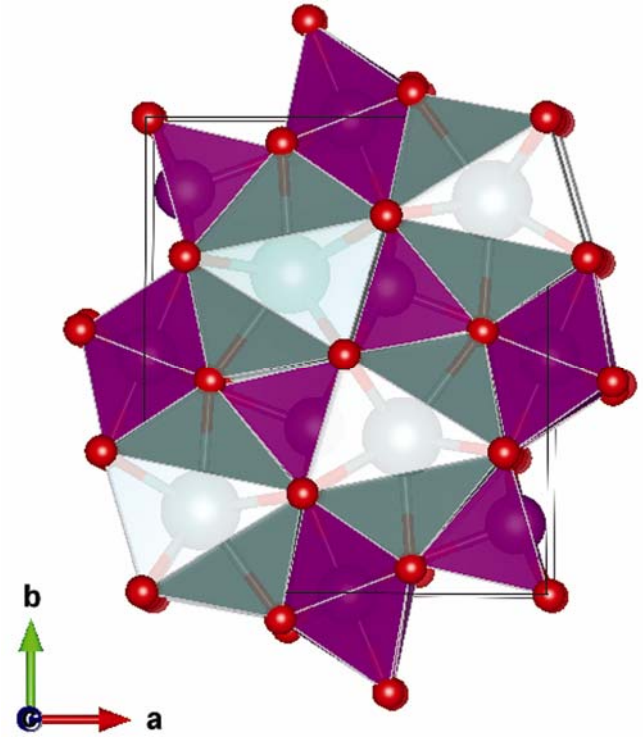

Figure 2. Structure of YMn_2O_5. Coordination polyhedra of Mn^{4+} and Mn^{3+} are violet octahedra and violet pyramids, respectively while Y^{3+} (grey spheres) are in coordination 8.

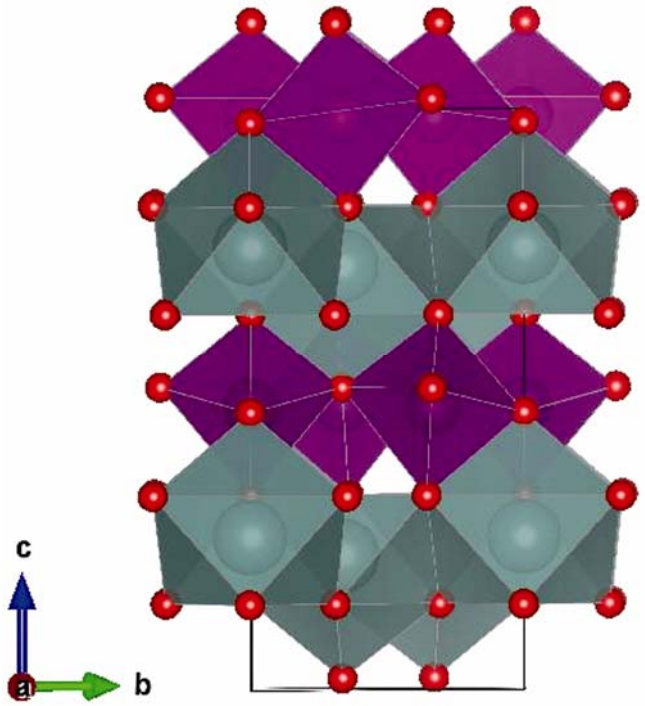

Figure 3. Structure of $YMnO_3$, where violet octahedra represent 6-fold coordination of Mn^{3+} and grey are coordination polyhedra for Y^{3+}.

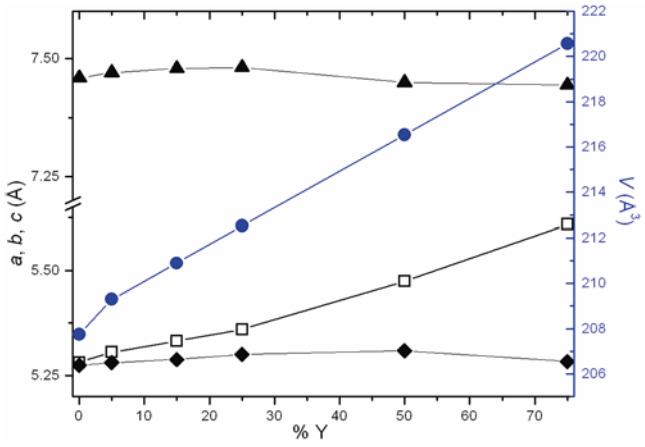

Figure 4. Influence of Y^{3+} amount on unit cell parameters: *a* (□), *b* (▲), *c* (◆) and unit cell volume (●).

of the Ca100 sample is 1·907 Å. This indicates the presence of Mn^{3+} and intrinsic oxygen vacancies even in the undoped perovskite. As expected, ⟨Mn–O⟩ distance increases with amount of yttrium, and goes from 1·904 Å in Ca95 sample up to 1·974 Å for the perovskite with highest amount of Y^{3+} and Mn^{3+} (Ca25).

Additionally, the influence of dopant concentration on octahedra deformations was analysed. The Jahn–Teller effect causes a regular octahedron to distort with the formation of two long and two short bonds [Mn–O(2)] in the *a*–*c* plane. Bonds of intermediate length, [Mn–O(1)] are directed towards *b*-axis. The distortion of the octahedra is defined in the way that the deviation of the Mn–O distances, r_i with respect to the average value, r is quantified:

$$\Delta = 1/n \sum \{(r_i - r/r\}^2 \times 10^3. \quad (1)$$

Interatomic distances, Mn–O inside octahedra for the perovskite phase in all investigated samples are shown in figure 5. First bar is for interatomic Mn–O1 distance, in *b* axis direction, and second and third bars represent distances Mn–O2 in the *a*–*c* plane. Also, calculated octahedra distortions parameters, Δ are given in the figure 5. According to this quantity, octahedra that are most distorted as the result of Jahn–Teller effect are in the perovskite of the Ca75 sample (figure 6(a)). $CaMnO_3$ also shows octahedral deformation phenomenon (table 2), and this indicates that there is some amount of Mn^{3+} in the structure and some amount of intrinsic oxygen vacancies as well. Octahedra net for the perovskite from the Ca100 sample is in figure 6(b). We also think that as mentioned by (Melo Jorge *et al* 2001), this compound may be considered as nonstoichiometric phase $CaMnO_{3-\delta}$.

Changes in angle values represent structural changes as a result of octahedral tilting. Angles Mn–O1–Mn and Mn–O2–Mn are in the ideal cubic perovskite structure

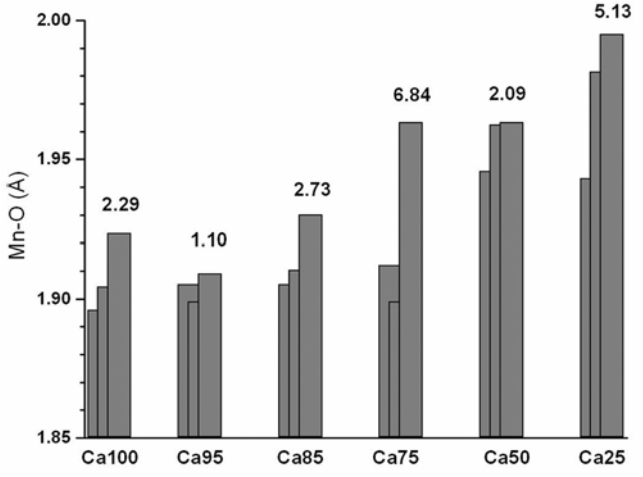

Figure 5. Interatomic distances Mn–O1 and Mn–O2 for perovskite phases in investigated samples. Quantity, Δ is given above each bar.

equal to 180°. As a result of increased octahedra tilting magnitude around all three axes, the angles in investigated perovskites differ from this value (table 2). Mn–O1–Mn angle indicates the magnitude of tilting around *b* axis and for investigated samples difference from 180° increases with increase in Y amount in the structure.

In general, tilting of BO_6 octahedra induce a distortion of AO_{12} polyhedra which can result in a decrease in the *A* site coordination number. The reduced coordination is due to the movements of some of the anions too far away from the cation and can not be considered as a part of the coordination sphere. Space group *Pnma* also permits migration of the *A* cation from its ideal site. Different coordination numbers (CN = 10, 9 and 8) have been reported to occur as a result of different tilt schemes (Mitchell 2002). The coordination polyhedra of cations occupying *A* site of the most ABO_3 orthorhombic perovskites is regarded as 8-fold rather than 12-fold, i.e., a four-fold antiprism with eight short *A*–O bonds in the first coordination sphere of the *A* cation. Four longer *A*–O bonds give rise to the second coordination sphere. Bond length analysis of the compounds synthesized shows that the *B* site cation enters the second coordination sphere of the *A* cation, as the *A*–O distances exceed the minimum *A*–*B* distance (table 2). If we apply criteria that *A*–*B* distance separates first and second coordination spheres, *A* cation in perovskite phase of the Ca100 sample has 12-fold coordination. In the perovskites from Ca95, Ca85 and Ca75 samples, *A* site cations are coordinated with 10 oxygen atoms. With further increase of *x*, the *B* cation moves closer to the *A* site coordination sphere, as demonstrated by the increase in the separation between the longest *A*–O bond and the *A*–*B* interatomic distance. Therefore, this results in 8-fold coordination number for *A* site cation in samples Ca50 and Ca25.

Additionally, coordination numbers can be evaluated by bond valence calculations. The bond valence (s_{ij}) associated with each cation–anion interaction is calculated using (2), where R_{ij} is the cation-anion distance:

$$s_{ij} = \exp\left(\frac{R_0 - R_{ij}}{B}\right). \quad (2)$$

The *B* parameter is empirically determined, but can often be treated as an universal constant with a value of 0·37 (Lufaso and Woodward 2001). R_0 is empirically determined for each cation–anion pair (Brown and Altermatt 1985; Brese and O'Keeffe 1991).

The atomic valences, V_i, of the *A* (Ca^{2+}, Y^{3+}) and *B* (Mn^{4+}, Mn^{3+}) cations are calculated according to (3) by summing the individual bond valences arround each cation:

$$\sum_j s_{ij} = V_i. \quad (3)$$

Bond valence calculations are given in table 2. For the calculation of the bond valences, we considered coordination

Table 2. Selected interatomic distances and angles for investigated perovskite phases.

	Ca100		Ca95			Ca85			Ca75			Ca50			Ca25		
		Ca^{2+}		Ca^{2+}	Y^{3+}		Ca^{2+}	Y^{3+}		Ca^{2+}	Y^{3+}		Ca^{2+}	Y^{3+}		Ca^{2+}	Y^{3+}
2 × Ca–O2	2·53(3)	0·218	2·36(2)	0·346	0·398	2·341(1)	0·365	0·420	2·329(1)	0·374	0·430	2·344(9)	0·366	0·422	2·384(1)	0·324	0·373
2 × Ca–O2	2·63(3)	0·167	2·58(2)	0·191	0·220	2·570(1)	0·196	0·225	2·596(1)	0·183	0·210	2·495(9)	0·241	0·277	2·438(1)	0·280	0·322
2 × Ca–O2	3·16(3)	0·039	2·58(3)	0·191	0·220	2·591(1)	0·185	0·213	2·568(1)	0·197	0·227	2·627(9)	0·166	0·192	2·646(1)	0·160	0·184
2 × Ca–O2	2·32(2)	0·385	3·11(2)	0·046	0·052	3·179(1)	0·038	0·043	3·220(1)	0·034	0·039	3·320(9)	0·026	0·029	3·411(1)	0·020	0·023
Ca–O1	2·98(4)	0·065	2·33(3)	0·375	0·431	2·346(2)	0·361	0·416	2·324(2)	0·381	0·439	2·245(2)	0·475	0·546	2·234(2)	0·486	0·059
Ca–O1	2·916(2)	0·078	2·465(2)	0·257	0·296	2·402(1)	0·309	0·355	2·426(1)	0·289	0·333	2·327(1)	0·379	0·436	2·353(2)	0·351	0·404
Ca–O1	2·32(4)	0·385	2·97(3)	0·066	0·077	2·976(2)	0·065	0·075	3·009(2)	0·060	0·069	3·155(2)	0·040	0·046	3·158(2)	0·040	0·046
Ca–O1	2·410(2)	0·302	2·910(1)	0·078	0·090	2·988(1)	0·063	0·073	3·007(1)	0·060	0·069	3·276(1)	0·029	0·033	3·390(2)	0·021	0·025
⟨Ca–O⟩	2·659		2·662			2·673			2·683			2·715			2·741		
FC. Ca^{2+}, Y^{3+}		2·448		2·324	2·674		2·366	2·721		2·366	2·722		2·521	2·901		2·466	2·838
FC. site *A*		2·448		2·345			2·419			2·444			2·695			2·726	
Exp. FC.		2		2·06			2·148			2·22			2·458			2·70	
2 × Mn–O2	1·920(1)	0·631	1·899(2)	0·674	0·687	1·910(1)	0·654	0·666	1·900(1)	0·674	0·687	1·960(9)	0·568	0·579	1·982(1)	0·539	0·550
2 × Mn–O2	1·906(1)	0·664	1·909(2)	0·653	0·675	1·930(1)	0·620	0·631	1·963(1)	0·562	0·573	1·964(9)	0·566	0·577	1·995(1)	0·520	0·530
2 × Mn–O1	1·896(5)	0·680	1·906(6)	0·656	0·668	1·905(3)	0·663	0·675	1·912(4)	0·650	0·663	1·944(5)	0·605	0·594	1·943(5)	0·598	0·609
⟨Mn–O⟩	1·907		1·904			1·915			1·925			1·956			1·974	3·314	3·378
FC. Mn^{4+} Mn^{3+}		3·95		3·966	4·06		3·874	3·944		3·772	3·846		3·478	3·5		3·359	
FC. site *B*		3·95		3·99			3·884			3·788			3·488			3·30	
Exp. FC.		4·00		3·94			3·852			3·78			3·542				
Ca–Mn shortest dist	3·231(2)		3·105(3)			3·090(3)			3·089(3)			3·068(2)			3·058(3)		
Mn–O1–Mn	159·22		157·13			157·551			156·048			146·341			146·529		
Mn–O2–Mn	154·26		158·72			155·60			154·95			152·47			151·31		
Microcrystalline size (Å)	529(1)*		677·4(9)*			1047·2 (9)*			510 (1)*			469·9(9)*			472(1)*		
Microstrain	0·633(1)*		1·830(3)*			2·707(1)*			2·7213(2)*			3·322(5)*			3·587(4)*		

*Values in brackets are a measure of the degree of anisotropy.

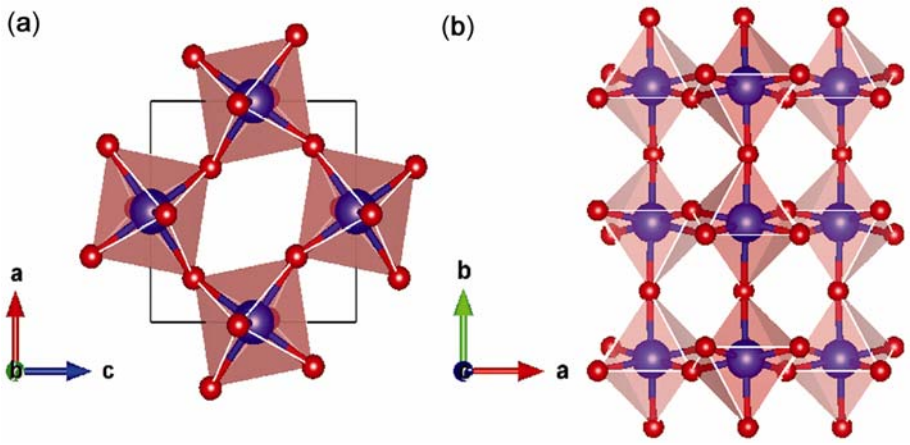

Figure 6. Distorted octahedra in perovskite of Ca75 sample (**a**) and octahedra net for perovskite phase in Ca100 sample (**b**).

Table 3. Atomic concentrations of yttrium in perovskite phases before and after sputtering (as).

	Y 3*d*		O 1*s*	
Atomic concentration (%)		as		as
Ca100	0	0	65·86	62·00
Ca95	1·75	1·76	65·57	62·38
Ca85	4·04	4·28	64·03	60·06
Ca75	5·06	5·50	63·81	59·25
Ca50	9·62	11·94	62·57	58·70
Y100	21·44	22·57	60·99	57·91

12 for the *A* site cation. This sum for Ca^{2+} is higher than 2+ in all samples, even in undoped perovskite, and it goes up to 2·726 in the Ca25 sample, where the amount of yttrium is highest. It is expected that Σs_{ij} should be equal to the formal charge (FC) of the *A* and *B* site cations. For example, if we consider perovskite phase in the Ca50 sample, and if amounts of Ca^{2+} and Y^{3+} are determined by refined occupation factors, then, we can calculate formal charge of the position *A* from the sum of individual bond valences as $x\Sigma s_{Ca} + (1-x)\Sigma s_Y = 0{\cdot}542 \times 2{\cdot}521 + 0{\cdot}458 \times 2{\cdot}901 = 2{\cdot}695$ Å. For calculating expected formal charge (Exp. FC) of the site *A*, we take charge 2+ for Ca and 3+ for Y, and their relation in site *A*. For the perovskite phase in Ca50 sample, this Exp. FC is 2·458 Å. In the case of undoped perovskite in the Ca100 sample, sum of the bond valences is higher (>20%) than expected formal charge +2. Reasons for this are the short distances Ca–O1 and Ca–O2.

In table 2, we can be seen that the distances *A*–O above 3 Å, contribute little to the sum of bond valences. If we disregard this bonds as a part of coordination sphere, coordination number of the *A* site cation would be 10 for perovskite phases in Ca100, Ca95 and Ca85 samples, and 8 in Ca75, Ca50 and Ca25 samples.

Sum of the bond valences is in good agreement with the formal charge of the *B* site cation, for all the samples. Mn valence state is in a good agreement with expected one. The presence of Mn^{3+} in doped perovskite phases decreases the valence state of Mn, as one can see in table 2.

XRPD line-broadening analysis was performed using the Rietveld method in conjunction with Warren–Averbach procedure in order to get crystallite size and lattice micro strain parameters. In the present approach, the grain size broadening was represented by a Lorentzian function, and micro strain broadening by a Gaussian function. The convolution of these functions is a Voigt function which is approximated by a modified Thompson–Cox–Hastings pseudo-Voigt (Young 1996). Obtained crystallite sizes are nanometric ranging from 450 to 1050 Å. Microstrain increases with increasing yttrium amount (table 2).

The best fit between calculated and observed X-ray diffraction patterns for each investigated sample is shown in figure 7, where all allowed Bragg reflections are shown by vertical bars. Inspecting the difference between the experimental and calculated profiles indicates good agreement.

By applying XPS method, the binding energy of a selected atomic level is correlated to a chemical environment of the investigated atom. Nanopowders were measured using XPS method before and after sputtering. The calculation of the standard atomic concentration provided a ratio of each component to the sum of the other elements considered in the data. The intensities of the binding energies for Mn (3*s*) electrons are too weak and can not be used for estimation of Mn^{4+}/Mn^{3+} relation. Mn (2*p*) electrons have identical binding energies in the samples; therefore, the valence states of Mn could not be discerned. Binding energies for Mn (2*s*) electrons are overlapped, and it is not clear what is the contribution of Mn^{4+} and Mn^{3+}. In order to follow the increase of yttrium concentration, we calculated atomic concentration of yttrium and oxygen before and after sputtering in all

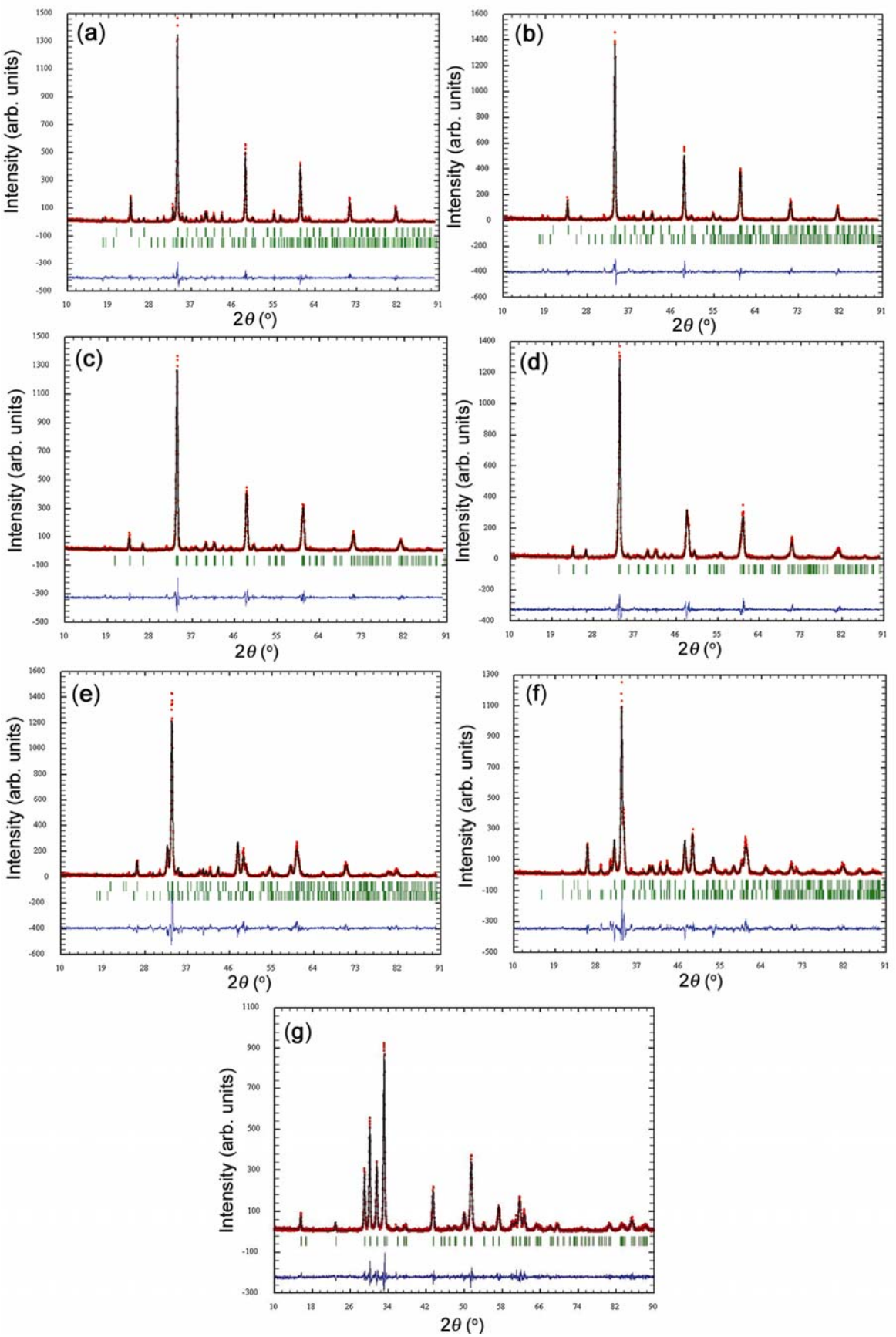

Figure 7. Rietveld diagrams for Ca100 (**a**), Ca95 (**b**), Ca85 (**c**), Ca75 (**d**), Ca50 (**e**), Ca25 (**f**) and Y100 (**g**) samples.

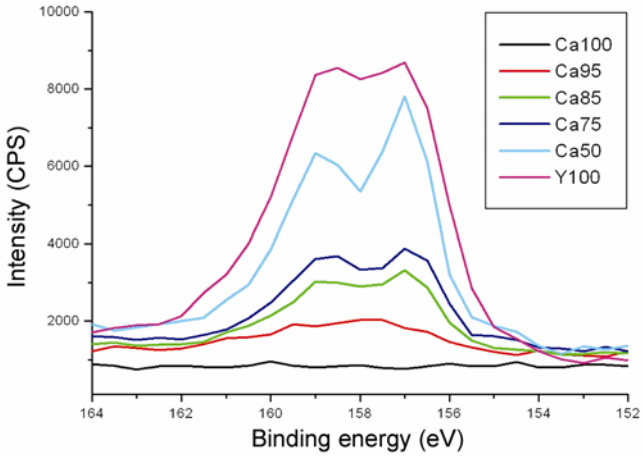

Figure 8. Yttrium (3*d*) XPS spectrum for investigated perovskite phases.

synthesized samples (table 3), except Ca25, since its second phase contains Y. XPS photoelectron peaks for Y (3*d*) electrons that were identified using line position tables (Moulder *et al* 1992) are given in figure 8. Since, sputtering may cause changes in the surface chemistry (table 3), so the chemical composition from the sputtered samples may not reflect the true composition. The amount of yttrium in the investigated nanopowders is estimated from the measurements before sputtering, and gave us the following compositions: $Ca_{0.92}Y_{0.08}MnO_3$ (Ca95); $Ca_{0.81}Y_{0.19}MnO_3$ (Ca85); $Ca_{0.76}Y_{0.24}MnO_3$ (Ca75); $Ca_{0.54}Y_{0.46}MnO_3$ (Ca50) and $Y_{1.05}MnO_3$ (Y100). Compositions of the perovskite phases calculated from the XPS results are in good agreement with the results obtained from refinement of occupation factors.

4. Conclusions

The series of nanosized $Ca_{1-x}Y_xMnO_3$ ($0 \le x \le 1$) solid solutions have been synthesized using modified glycine nitrate procedure (MGNP). Structures and microstructures for investigated perovskites have been determined by Rietveld refinement of X-ray powder diffraction data (XRPD). Investigated perovskite phases adopt space group *Pnma*, where only undoped $CaMnO_3$ exhibits $GdFeO_3$ or *O* type of the perovskite structure and all other perovskite phases have $REMnO_3$ (RE = La–Dy) or *O′* type of perovskite consisting of distorted coordination polyhedra at both *A* and *B* cations.

As a result of the substitution of Y^{3+} for Ca^{2+} in *A* site, and the reduction of Mn^{4+} to a larger Mn^{3+} in *B* site, the increase of unit cell volumes and the average *A*–O and *B*–O distances is observed in each of the measured perovskites. Also, the presence of Mn^{3+} cation introduces the Jahn–Teller effect, which results in distortion of octahedra around *B* site cation, whereby this distortion is the most pronounced in the perovskite phase of the Ca75 sample.

We observed that the *B* site cations are inside the *A* site cations coordinaton sphere in each of the perovskite phase, except for undoped $CaMnO_3$, and in this way 12-fold coordination of the *A* site cation is reduced to 8-fold coordination. In addition, sum of the bond valences is higher than the formal charge of the *A* site cation in each of the measured samples, but it is in a good agreement for *B* site cation. The coordination of the *A* site cation, estimated from the bond valence analysis, changes throughout the series from 10, for compounds with less yttrium ($0 \le x \le 0{\cdot}15$) to 8, for compounds with higher concentration of yttrium ($0{\cdot}25 \le x \le 0{\cdot}75$).

The obtained powders are in nanometric range, which is confirmed by the microstructural analysis. The obtained average amount of yttrium using the XPS method and Rietveld refinement are in good agreement. The study also concluded that neither of two oxidation states of manganese in nanostructured yttrium-doped $CaMnO_3$ are distinguishable by XPS.

Acknowledgements

This paper has been financially supported by the Ministry of Science of the Republic of Serbia, as a part of project no. III45012. Mr Mitsuharu Konuma is acknowledged for performing XPS measurements and Dr Snezana Boskovic for useful discussions.

References

Aliaga H, Causa, M T, Alascio B, Salva H, Tovar M, Vega D, Polla G, Leyva G and Konig P 2001 *J. Magn. Magn. Mater.* **226–230** 791

Blasco J, Garcia J, De Teresa J M, Ibarra M R, Algarabel P A and Marquina C 1996 *J. Phys.: Condens. Matter* **8** 7427

Blasco J, Ritter C, Garcia J, De Teresa J M, Perez-Cacho J and Ibarra M R 2000 *Phys. Rev.* **B62** 5609

Boskovic S, Dukic J, Matovic B, Zivkovic Lj, Vlajic M and Krstic V 2008 *J. Alloys Compd.* **463** 282

Boskovic S B, Matović B Z, Vlajić M D and Krstić V D 2007 *Ceram. Int.* **33** 89

Brese N E and ÓKeeffe M 1991 *Acta Cryst.* **B47** 192

Brown I D and Altermatt D 1985 *Acta Cryst.* **B41** 244

Dlouha M, Vratislav S, Jirak Z, Hejtmanek J, Knizek K and Sedmidubsky D 2002 *Appl. Phys.* **A74** S673

Dukic J, Boskovic S and Matovic B 2009 *Ceram. Int.* **35** 787

Hibble S J, Cooper S P, Hannon A C, Fawcett I D and Greenblatt M J 1999 *J. Phys. Condens. Matter* **11** 9221

Iliev M N, Abrashev M V, Lee H G, Popov, V N, Sun Y Y, Thomson C, Meng R L and Chu C W 1998 *Phys. Rev.* **B57** 2872

Ling C D, Neumeier J J and Argyriou D N 2001 *J. Solid State Chem.* **160** 167

Lufaso M W and Woodward P M 2001 *Acta Cryst.* **B57** 725

Lukaszewicz K and Karut-Kalicinska J 1974 *Ferroelectrics* **7** 81
Melo Jorge M E, Correia dos Santos A and Nunes M R 2001 *Int. J. Inorg. Mater.* **3** 915
Mitchell R H 2002 *Perovskites: modern and ancient* (Canada, Thunder Bay, Ontario: Almaz Press)
Mitchell R H and Liferovich R P 2005 *J. Solid State Chem.* **178** 2586
Moulder J F, Stickle W F, Sobol P E and Bomben K D 1992 *Handbook of X-ray photoelectron spectroscopy* (Minnesota, USA: Physical Electronics, Inc. Perkin-Elmer Corp.)
Mueller O and Roy R 1974 *The major ternary structural families* (Berlin: Heidelberg; New York: Springer)
Nagabhushana B M, Chandrappa G T, Sreekanth Chakradhar R P, Ramesh K P and Shivakumura C 2005 *Solid State Commun.* **136** 427
Raveau B, Maignan A, Martin C and Harvieu M 1998 *Chem. Mater.* **10** 2461
Rodriguez-Carvajal J 1990 *Collected abstract of powder diffraction meeting, Toulouse*, p. 127
Shannon R D 1976 *Acta Cryst.* **A32** 751
Woodward P M, Vogt T, Cox D E, Arulraj A, Rao C N R, Karen P and Cheetham A K 1998 *Chem. Mater.* **10** 3652
Wunderlich F, Leisegang T and Weissbach T 2010 *Phys. Rev.* **B82** 014409
Van Aken B B, Meetsma A and Palstra T T M 2001 *Acta Cryst.* **C57** 230
Vecherskii S I, Konopelko M A, Esina N O and Batalov N N 2002 *Inorg. Mater.* **38** 1270
Vega D, Polla G, Leyva A G, Konig P, Lanza H and Esteban A 2001 *J. Solid State Chem.* **156** 458
Young R A 1996 *The rietveld method. IUCr Monographs on Crystallography 5* (Oxford, UK: University Press) p. 132
Zagorac J, Boskovic S, Matovic B and Babic-Stojic B 2010 *Sci. Sint.* **42** 221